Dalton Transactions

ROYAL SOCIETY OF CHEMISTRY

PAPER

View Article Online
View Journal | View Issue

Cite this: *Dalton Trans.*, 2026, **55**, 1473

Tuning chemical properties on ruthenium(II) complexes through PEGylation of N-heterocyclic carbene ligands

Oscar Barrios,[a,b] Tamara Rodriguez-Prieto,[a] Alicia Bort,[c] Elżbieta Okła,[d] Marek Maly,[e] Miriam Chavez,[f] Alberto Escarpa,[f] Maksim Ionov,[d,g] Maria Bryszewska,[d] Jesús Cano,[a,b,h] Inés Díaz-Laviada *[c] and Rafael Gómez *[a,b,h]

A series of ruthenium complexes containing a N-heterocyclic carbene (NHC) ligand with three types of PEG substituents were synthesized, and their molecular modeling and electrochemical characterization were performed. Their interaction with BSA was also investigated using fluorescence quenching, circular dichroism, DLS, and zeta potential measurements. The PEG fragments strongly influenced reactivity, modulating both biomolecular interactions and chemical kinetics. Although all complexes exhibited identical reduction potentials, larger PEG chains imposed steric hindrance around the metal center, leading to slower mass transport, hindered heterogeneous electron transfer, and reduced hydride formation. Interaction studies with BSA indicated predominantly static quenching, consistent with stable adduct formation, while larger PEG units also introduced dynamic contributions. This behavior suggests that BSA can act as a carrier, facilitating plasma transport, or support their application as artificial nanozymes. Importantly, the Ru–PEG systems were generally non-toxic and displayed catalytic activity in hydrogen transfer reactions, including ketone and NAD^+ reduction. This activity was further enhanced when cationic micelles or BSA were employed as carriers. Overall, the non-toxic nature, catalytic potential, and ability to interact with proteins highlight Ru–PEG complexes as promising candidates for intracellular catalytic applications.

Received 6th October 2025,
Accepted 17th December 2025

DOI: 10.1039/d5dt02391b

rsc.li/dalton

Introduction

Cancer has become one of the greatest threats to human life, prompting extensive efforts to synthesize therapeutic agents for precise and efficient treatment while minimizing off-target toxicity.[1] To achieve optimal therapeutic efficacy for *in vivo* experiments, different physiological barriers must be overcome: (i) prolonged circulation in the bloodstream, (ii) efficient accumulation in cancerous tissues, for example, *via* the Enhanced Permeability and Retention (EPR) effect, (iii) effective penetration into tumor tissue, (iv) cellular internalization by tumor cells, and (v) intracellular drug release.[2] Additionally, drugs can interact with serum proteins, particularly albumin, the most abundant plasma protein, accounting for approximately 60% of total plasma protein content, and thereby altering their pharmacokinetics and pharmacodynamics.[3] In this context, camouflage of the anticancer drugs may be considered as an alternative route to enhance their biological properties. One approach involves the use of carriers functionalized with hydrophilic biopolymers to improve drug stability and biocompatibility. These polymers have demonstrated significant potential in reducing non-specific protein interactions and preventing rapid clearance from the circulating system. Among these, poly(ethylene glycol) (PEG) has been widely employed for such purposes, with its conjugation to therapeutic agents achieved through a chemical process known as PEGylation.[4,5] PEGylation offers several advantages, including increased water solubility, reduced clearance by the reticuloendothelial system, prolonged circulation time,

[a]*University of Alcalá, Department of Organic and Inorganic Chemistry and Research Institute in Chemistry "Andrés M. Del Río" (IQAR), Madrid, Spain. E-mail: rafael.gomez@uah.es; Tel: (+34) 91 8854685*
[b]*Networking Research Center on Bioengineering, Biomaterials and Nanomedicine (CIBER-BBN), Madrid, Spain*
[c]*University of Alcalá, Biochemistry and Molecular Biology Unit. Department of Systems Biology and Research Institute in Chemistry "Andrés M. Del Río" (IQAR), Madrid, Spain. E-mail: ines.diazlaviada@uah.es; Tel: (+34) 91 8855141*
[d]*Faculty of Biology and Environmental Protection, Department of General Biophysics, University of Lodz, Pomorska 141/143, Lodz 90–236, Poland*
[e]*Department of Physics, Faculty of Science, University of Jan Evangelista Purkyně in Ústí nad Labem, Pasteurova 15, 400 96 Ústí nad Labem, Czech Republic*
[f]*University of Alcalá, Department of Analytical Physical-Chemistry and Chemical Engineering and Research Institute in Chemistry "Andrés M. Del Río" (IQAR), Madrid, Spain*
[g]*Collegium Medicum, Faculty of Medicine, Mazovian Academy in Plock, Pl. Dabrowskiego 2, Plock 09-402, Poland*
[h]*Ramón y Cajal Health Research Institute (IRYCIS), IRYCIS, Madrid 28034, Spain*

enhanced tissue targeting, decreased enzymatic degradation, and reduced immunogenicity, as the result of a "stealth" effect by preventing adsorption or interaction with proteins.[6,7] Therefore, all these features have been shown to optimize the pharmacokinetics and pharmacodynamics of drugs.[8] In addition, PEG polymers can be liquid (below 1000 Da), waxy solids (1000–2000 Da) or crystalline solids (above 2000 Da). These molecular weight differences affect properties such as solubility and viscosity, thereby influencing their behaviour in catalytic and biomedical processes.

With this in mind, transition metal complexes have been PEGylated for applications in aqueous-phase catalysis[9–13] and biomedicine, benefiting from increased hydrophilicity, water solubility, and cellular permeability.[14,15] In catalysis, PEG-functionalized metal complexes offer several advantages. The PEG chain improves solubility in diverse solvents, including water, facilitating reactions in both aqueous and organic media or as a stabilizing ligand, preventing the aggregation of catalytic species and enabling recyclability. Additionally, PEG can act as a steric and electronic modifier, tuning the activity and selectivity of metal centers. PEG has been covalently linked to transition metal complexes originally directed towards catalytic processes,[9–11] with very few examples containing the Ru–NHC fragment.[13,16] In biomedicine, the "stealth" behavior mentioned above can also mitigate the toxicity often associated with metal complexes, broadening their clinical potential. Applications range from PEGylated platinum complexes used in cancer therapy to metal-based contrast agents for magnetic resonance imaging (MRI).[14,17] As far as we are concerned, only one example has been recorded in the literature for NHC–metal complexes for biomedical applicatons.[15]

Recently, a new concept for the design of anticancer agents and therapeutic routes has emerged combining the catalytic properties of metal complexes and their implication in cancer.[18,19] This integrative approach offers a promising avenue for the development of new cancer treatments. Many metal complexes (*e.g.*, ruthenium, gold, iridium) participate in redox reactions, which can disrupt cancer metabolism or induce apoptosis by generating reactive oxygen species (ROS) or just simply creating an imbalance of the redox homeostasis. Cellular redox homeostasis is controlled by several reducing agents (mainly glutathione (GSH), thioredoxin reductase (TrxR), nicotinamide adenine dinucleotide (NADH)). Therefore, altering their intracellular concentrations may have serious consequences in the cell viability.[19–21] These complexes can act as catalysts inside cancer cells, promoting redox reactions that generate reactive oxygen species (ROS). The increase in ROS can induce oxidative stress, leading to apoptosis in malignant cells. Some metal complexes can inhibit key enzymes involved in maintaining the cellular redox balance, such as TrxR which disrupts the ability of cancer cells to neutralize oxidative stress, contributing to their death. Conversely, the induction of reductive stress is characterized by excess accumulation of reducing molecules (*e.g.*, NADH, thioredoxin or GSH), overpassing the activity of endogenous oxidoreductases. Unlike oxidative stress, reductive stress is not sufficiently described, and little attention has been paid in this direction. Reductive stress impairs cellular signaling and function, leading to disruption of mitochondrial homeostasis, decreased metabolism, resistance to anticancer therapies, alteration of the formation of disulfide bonds in proteins, and finally being harmful to cells. This reductive state can be achieved using transition metal complexes as catalysts by using transfer hydrogenation (TH).[19,20]

TH is a safer alternative to H_2-based hydrogenation, using easy handling donor molecules like alcohols or formic acid to reduce unsaturated substrates. It avoids pressurized hydrogen and allows the use of stable, easy-to-handle catalysts. Several late transition metals[22,23] are used, with ruthenium, especially NHC-based complexes, being the most widespread studied.[24]

In this work, we present the synthesis and characterization of Ru(II)–NHC complexes containing different PEG units and their behavior in catalytic TH processes as well as their anticancer behavior. The modulation of these properties as a function of the PEG fragment size will be studied as a preliminary step for subsequent investigations within the cell.

Results and discussion

Synthesis and characterization

Imidazolium ligands containing a short PEG unit with a molecular weight of 147 Da (PEG_{147}) were recently described by our research group.[15] Very briefly and focusing on commercially available 4,5-dichloroimidazole, PEG containing imidazole (**L1**), imidazolium (**L2**) and the corresponding Ru(II) complex [Ru(II)(*p*-Cym)(NHC_{147})Cl_2] (**1**) were synthesized elsewhere. Following the same procedure, from commercially available 4,5-dichloroimidazole, imidazolium ligands with PEG_{500} and PEG_{2000} were prepared. PEGylation of 4,5-dichloroimidazole by using mesylated PEG ($MsOPEG_nMe$) (n = 500 (**L3**) and n = 2000 (**L4**)) afforded the imidazole ligands **L5** and **L6** *via* nucleophilic substitution. Subsequent reactions with MeI gave rise to the imidazolium systems **L7** and **L8** through *N*-quaternization in good yields (see Scheme 1).

The ^{1}H and ^{13}C NMR spectra of ligands **L7** and **L8** are consistent with the structures proposed and analogous to the imidazolium ligand containing PEG_{147} (**L2**) synthesized elsewhere.[15] A low field resonance around 11 ppm was observed for the imidazolinium proton, along with a signal at *ca.* 139 ppm in the ^{13}C NMR for the corresponding C atom (see Fig. S1–S6). Although these signals are not expected to be affected by the length of the PEG chain, a slight shift to higher ppm may be observed in both types of signals as the weight of the PEG fragment increases compared to the ligand **L2** (see Table 1), suggesting subtle electronic differences.

Respecting to the presence of the PEG unit bound to the NHC fragment, this can be described by a set of signals, being the more illustrative the methylene groups in the fragment –NCH_2CH_2O– located as triplets at *ca.* 4.58 (–NCH_2–) and 3.99 (–OCH_2–) ppm. The Me group, also bound to the NHC ligand, appeared at 4.06 ppm. In both cases, negligible differences were observed.

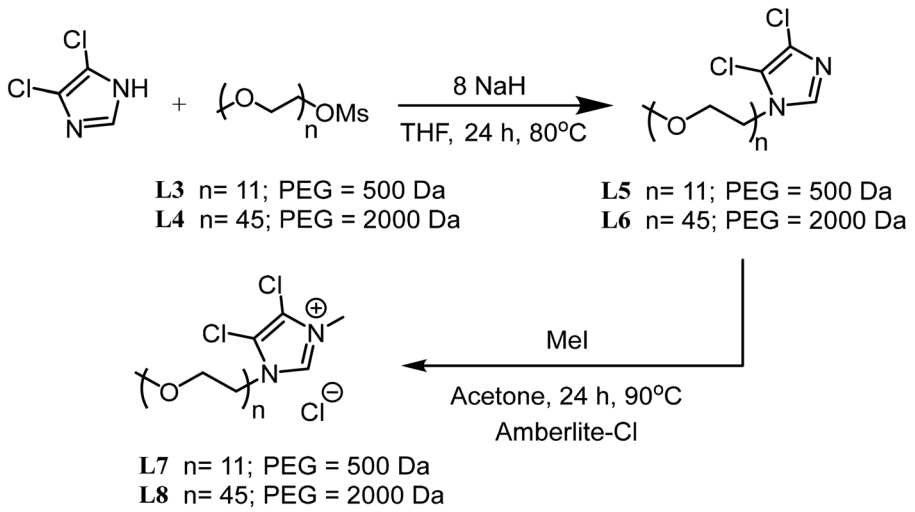

L3 n= 11; PEG = 500 Da
L4 n= 45; PEG = 2000 Da

L5 n= 11; PEG = 500 Da
L6 n= 45; PEG = 2000 Da

L7 n= 11; PEG = 500 Da
L8 n= 45; PEG = 2000 Da

Scheme 1 Synthetic route in the formation of PEGylated imidazole (**L5** and **L6**) and imidazolium (**L7** and **L8**) precursors.

Table 1 Selected ^{1}H and ^{13}C NMR signals of ligands **L2**, **L7** and **L8**

Group	**L2** (PEG_{147})	**L7** (PEG_{500})	**L8** (PEG_{2000})
C**H** (Imid-2′)	11.03	11.13	11.18
C**H**$_3$ (Me-Imid)	4.05	4.06	4.06
N–C**H**$_2$–PEG_n	4.58	4.58	4.59
O–C**H**$_2$–PEG_n	3.96	3.99	3.99
CH (Imid-2′)	137.6	139.1	139.1

The [Ru(II)(*p*-Cym)(NHC_{PEG})Cl_2] complexes were obtained easily in a one-pot reaction by activating imidazolium ligands **L7** and **L8** with Ag_2O followed by transmetallation with [Ru(*p*-Cym)Cl_2]$_2$. This procedure leads to the complexes [Ru(*p*-Cym)(NHC_{PEG})Cl_2], where PEG = 500 (**2**); 2000 (**3**), as red brown oils in good yields (see Scheme 2), in a similar way to that performed by **L2** to produce [Ru(*p*-Cym)(NHC_{147})Cl_2] (**1**) elsewhere.[15]

Several features were observed in the NMR spectra that confirm the complexes formation (see Fig. S7 and S8) in analogy with the data obtained for complex **1**.[15] Briefly, the CH_2 groups of the N–CH_2CH_2O– fragments gave rise to diastereotopic protons appearing as separate broadened multiplets, being more evident for the CH_2 of the PEG chain bonded to the N atom and due to the lack of rotation in the Ru–C bond of the NHC ligand.[25,26] The two H of the methylene group attached to N appeared at *ca*. 5.2 and 4.3 ppm as diasterotopic atoms. For the cymene ligand, four broad resonances were also registered in the range 5.8–5.00 ppm. For complex **1**, this set of signals narrowed and became well-defined below 0 °C. The NMR data were supported by ESI-MS for complex **2**, which did not show molecular peaks but instead revealed a peak corresponding to the easy loss of a chlorine atom $[M - Cl]^+$ (see Fig. S7). The systematic loss of a Cl atom aligns with the tendency to form charged species in solution in the presence of certain ligands.[15] A certain degree of polydispersity is observed in the mass spectra, which is attributed to the inherent polydispersity of the commercial PEG_{500} and retained in the starting materials **L3** and **L7**. For complex **3**, the large molecular weight and higher polydispersity of the commercial PEG_{2000} prevented obtaining accurate results even in the corresponding ligands **L4** and **L8**.

Molecular modeling

To obtain detailed structural information about the conformations of Ru–PEG complexes in water, these systems were first simulated in vacuum and subsequently in explicit water using molecular dynamics. The primary goal was to determine how the polymeric PEG segment behaves in water and how

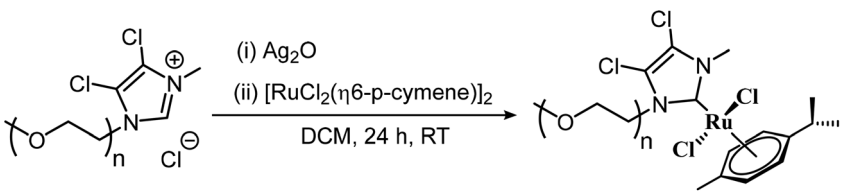

L7 n = 11, PEG = 500 Da
L8 n = 45, PEG = 2000 Da

2 n = 11, PEG = 500 Da
3 n = 45, PEG = 2000 Da

Scheme 2 Synthetic route for the formation of [Ru(II)(*p*-Cym)(NHC_{PEG})Cl_2] metal complexes (**2** and **3**).

this behavior changes with the polymer length. The simulations revealed that at lengths of 3 (147 Da) and 11 (500 Da) monomer units, the PEG chain adopts a rather extended conformation, whereas in the case of 45 monomer units (2000 Da), the polymer exhibits a strong tendency to wrap around the rigid part of the molecule containing the central Ru atom (see Fig. 1 and S9). This wrapping may reduce the accessibility of the Ru atom for interactions with other molecules or to slow down the reaction rates.

The structure of the solvated Ru–PEG molecules was analyzed using radial distribution functions (see Fig. 2 and 3). Furthermore, the radii of gyration of these solvated molecules were calculated (see Table 2). The radius of gyration (R_g) of the molecule is defined as the square root of the mass-weighted mean of the squared distances of all atoms from the center of mass of the molecule. It provides a measure of how mass is spatially distributed around the center of mass. The maximum dimension of the solvated molecules observed in the analyzed conformations is evident from Fig. 3, *i.e.* about 20 Å for Ru–PEG_{147} (**1**), about 27 Å for Ru–PEG_{500} (**2**), and around 26 Å for Ru–PEG_{2000} (**3**). These values provide insight into how solvent-accessible size and steric effects influence its reactivity. A larger value may indicate slower diffusion and reduced accessibility, while a smaller value may favor faster interactions.

Electrochemical characterization

The electrochemical performance of the synthesized ruthenium-based complexes (**1–3**), which include PEG chains of three different length within their structure, was investigated using cyclic voltammetry (CV). CV is usually employed to study the ability of a molecule to perform electron transfer and properties such as its prooxidant activity or transfer hydrogenation (TH) reactions can be estimated from this study. The cyclic voltammograms of complexes **1–3** were carried out in 0.1 M NaCl/water solutions at Ag/AgCl working electrode and at a scan rate of 0.25 mV s^{-1}. A prooxidant generally acts as an elec-

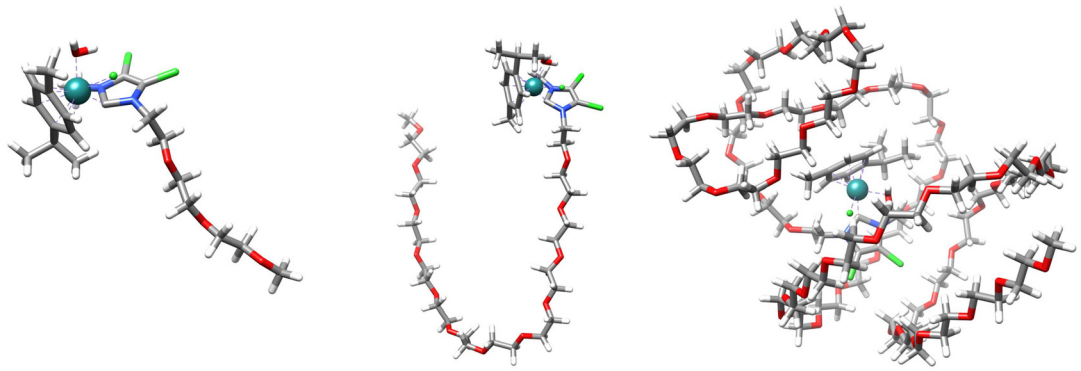

Fig. 1 Visualisation of simulated molecular structures. PEG_{147} (left), PEG_{500} (middle), PEG_{2000} (right). Colors: C – grey; O – red; H – white; N – blue; Cl – green; Ru – dark cyan (sphere).

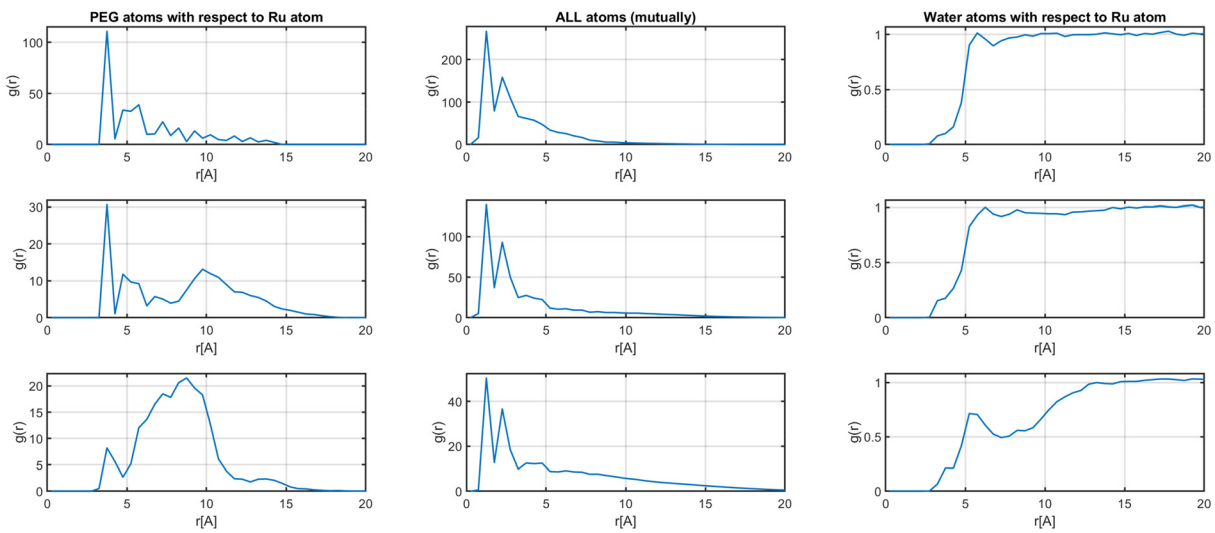

Fig. 2 Radial distribution functions (relative density profiles (RDF)) of selected atoms. RDF of PEG atoms with respect to Ru atom (first column), RDF of all molecule atoms (second column), RDF of water atoms with respect to Ru atom (third column). PEG_{147} (top), PEG_{500} (middle), PEG_{2000} (bottom).

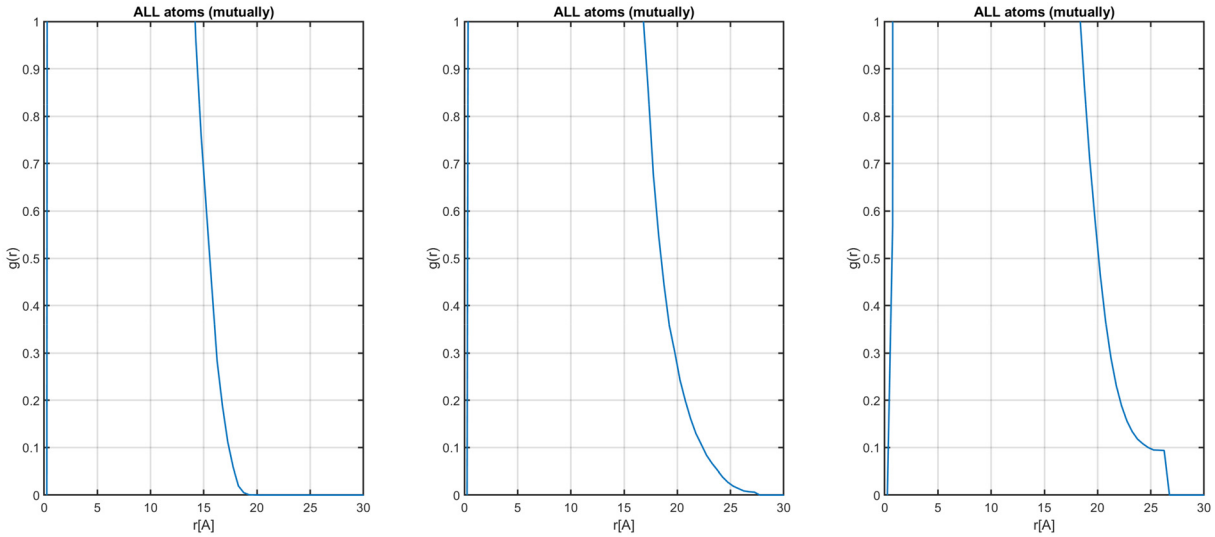

Fig. 3 Detail of radial distribution functions of all atoms of Ru–PEG complexes, to obtain information about the maximum distance of atoms in these molecules. PEG_{147} (left), PEG_{500} (center), PEG_{2000} (right).

Table 2 Radius of gyration R_g. The standard deviation is given in parentheses

Molecule	R_g [Å]
PEG_{147}	4.74 (0.08)
PEG_{500}	7.72 (0.32)
PEG_{2000}	9.00 (0.25)

tron-accepting agent (oxidizing agent) or promotes conditions that lead to the generation of electron-accepting species. In CV, the prooxidant behavior of the Ru(II) complex is reflected in its redox properties (Fig. 4). The complex can be readily reduced to Ru(I) (around −0.8 V) and subsequently oxidized to Ru(II), as evidenced by the consistent peak intensity and separation. The analysis of the anodic peak potential (E_{pa}) position, intensity (i_{pa}), and peak-to-peak separation with respect to the cathodic peak (E_{pc}) position (ΔE_p, reversibility) may provide insights for the prooxidant capacity or their involvement in TH processes. From these parameters, the diffusion coefficient (D_0) and the heterogeneous electron transfer (HET) rate constant (k_0) can be determined.

Prior to the evaluation of the above-mentioned parameters, complete cyclic voltammograms were recorded (Fig. 4). For **1** and **2**, a clear redox couple was found around $E_{1/2} = -0.8$ V (*vs.* Ag/AgCl) (see Fig. 4A). At such negative potentials, oxygen reduction is usually observed, therefore solutions were deoxygenated before the experiments (see Fig. 4B). Complex **3** does not present signals that could be attributed to a quasi-reversible redox process. This may be related to the considerably longer PEG chain wrapping the metal complex, which hinders access to the ruthenium center embedded within the structure,

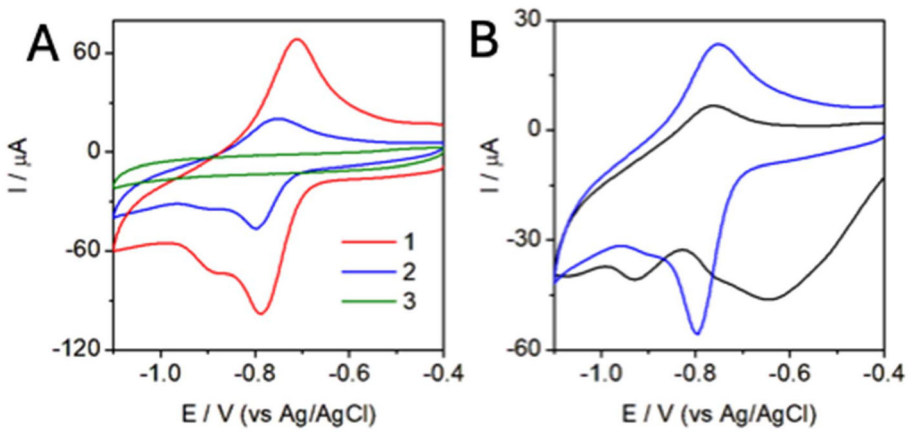

Fig. 4 (A) Cyclic voltammograms recorded for the reduction process of **1** (red), **2** (blue), and **3** (green) (from −0.4 to −1.1). (B) Signals recorded for **2** in the presence of oxygen (black) and once the solution has been deoxygenated (blue). All measurements were recorded in NaCl 0.1 M.

as suggested by molecular modelling, thereby restricting the electron-transfer redox process.

Thus, electrochemical parameters could only be determined for two of the three molecules studied, as summarized in Table 3. The reduction potentials found for **1** and **2** are very similar, as expected. Kubiak and coworkers demonstrated that the hydride donor strength (thermodynamic hydricity) increases linearly as the reduction potentials of a series of related complexes become more negative.[27] Considering that the reduction potentials of complexes **1** and **2** are essentially the same within experimental error, no significant differences are expected in their ease of reduction or hydride donor behavior. Although the reduction peak potentials of complexes **1** and **2** remain essentially unchanged, their oxidation peaks display significant displacement, consistent with distinct ligand effects on the oxidised Ru(III) state. Further discussion and relevant references can be found in the SI (see section S6). Therefore, both complexes can be regarded as essentially equivalent in terms of hydricity and the ease of forming the M–H bond. However, quite different behaviour is exhibited by the complexes **1** and **2**, which is evidenced by the determination of the D_0, and k^0. These values can be obtained from the study of electroactive species in solution as a function of the scan rate in cyclic voltammetry (Fig. 5).

If the recorded intensities for the two complexes under the same conditions are compared, the intensities of **1** fall to less than half compared to those of **2**, again highlighting the effect of PEG size. The diffusion coefficient is one of the most important characteristics of electroactive moieties in a molecule. Environmental variables greatly affect such parameters, including the electrolyte composition, temperature, and pressure. However, knowing its exact value seems to be essential for the understanding of electroactive species. The following eqn (1), known as Randles–Sevcik equation, describes the effect of scan rate on the peak current i_p for a CV measurement at 25 °C,

$$i_p = 2.69 \times 10^5 \cdot n^{3/2} \cdot A \cdot C \cdot D_0^{1/2} \cdot v^{1/2} \quad (1)$$

where i_p is the peak current of the redox reaction, n is the number of electrons involved, F is the Faraday's constant in (C mol^{-1}), D_0 is the diffusion coefficient (cm^2 s^{-1}), A is the area of the electrode (cm^2) and C is the concentration of the redox molecule (mol cm^{-3}). The Randles–Sevick plot, that is, peak intensity *vs.* square root of the scan rate, confirms that a diffusion control process is being produced (Fig. 6). In general terms, higher diffusion coefficients are related to easier movements of the reagents through the solution. Thus, it is expected that **1** exhibits the highest value of D_0. This could indicate that the presence of the pegylated chain hinders the electronic transfer of the Ru(II)/Ru(I) centers of the molecular chain.

The improved electron transfer in **1** was also confirmed by heterogeneous electron transfer (HET) using the Nicholson method (eqn (2)). The Nicholson's treatment is employed for the evaluation of the heterogeneous standard rate constant k^0

Table 3 Electrochemical parameters obtained from the analysis of the complexes **1** and **2**

Complex	E_a[a] (V)	i_a[b] (μA)	E_c[a] (V)	i_c[b] (μA)	ΔE[c] (mV)	D_O[d] (cm^2 s^{-1})	k^0[e] (cm s^{-1})
1	−0.71 ± 0.01	63 ± 2	−0.79 ± 0.02	68 ± 2	78	(1.2 ± 0.1) × 10^{-4}	0.11 ± 0.02
2	−0.75 ± 0.02	23 ± 0.18	−0.81 ± 0.02	27 ± 0.18	76	(0.8 ± 0.1) × 10^{-4}	0.071 ± 0.008

[a] Anodic peak potential. [b] Anodic intensity. [c] Peak-to-peak separation. [d] Diffusion coefficient. [e] Electron transfer rate constant. a, b, c were extracted from CV at 25 mV s^{-1}.

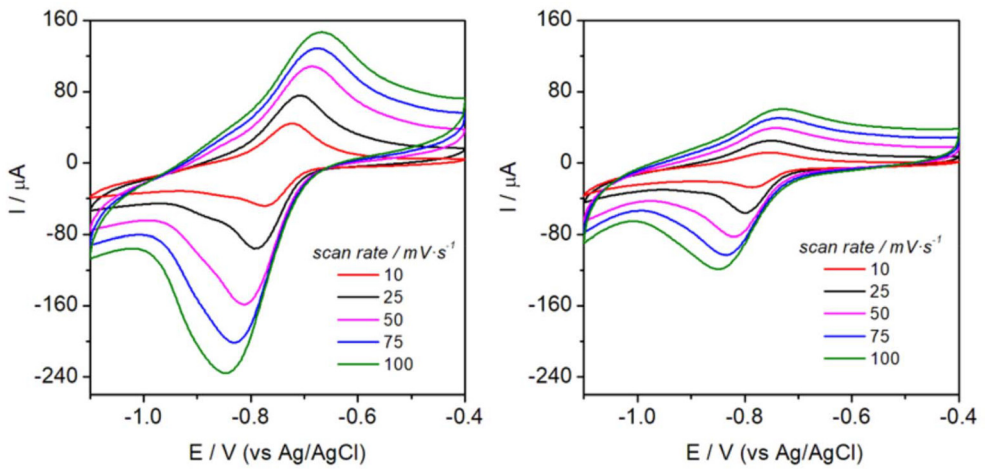

Fig. 5 Cyclic voltammograms for complexes **1** (left) and **2** (right) recorded at different scan rates. Measurements recorded in NaCl 0.1 M.

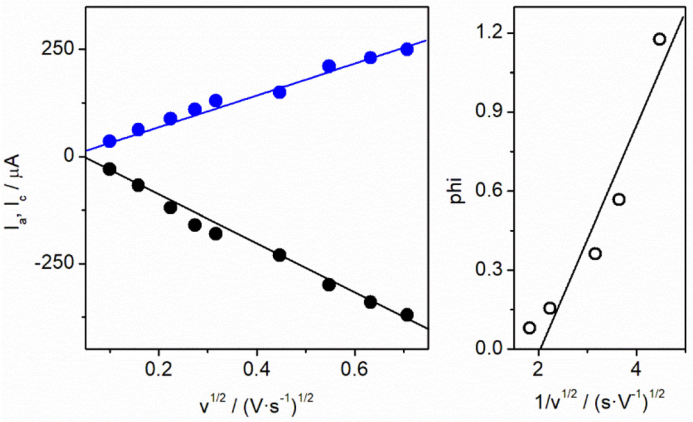

Fig. 6 Determination of the diffusion coefficient (left) and HET (right) for **1** complex in aqueous 0.1 M NaCl solution. [**1**] = 10 mM.

of electron transfer from cyclic voltammetry measurements. It relates the peak-to-peak separation with k^0 and the dimensionless parameter Ψ

$$\Psi = k^0 \left(\frac{n\pi D_0 F v}{RT}\right)^{-\frac{1}{2}} \quad (2)$$

where: k^0 is the heterogeneous rate constant (cm s^{-1}), D_0 is the diffusion coefficient (cm^2 s^{-1}), v is the scan rate (V s^{-1}), R is the ideal gas constant (J mol^{-1} K^{-1}), n is the number of electrons, F is the Faraday's constant in (C mol^{-1}), T is the temperature (K), and Ψ is the Nicolson dimensionless number. The kinetic parameter Ψ is tabulated as a function of ΔE_P at a set temperature (298 K) for a one-step, one electron process with a transfer coefficient α, equal to 0.5. Similar to the D_0 value, the complex **1** exhibits faster electron transport than complex **2** (0.11 *vs.* 0.07 cm s^{-1} respectively in Table 3). The higher diffusion coefficient (D_0) and standard heterogeneous electron transfer rate constant (k_0) observed for complex **1** relative to complex **2** indicate not only a faster mass transport but also a more facile interfacial electron transfer. Provided that hydride transfer follows electron transfer in the overall mechanism, these features could suggest a lower activation barrier and higher kinetic hydricity for complex **1**, thereby rationalizing its faster hydride transfer kinetics. These results can be tentatively extended to complex **3**, for which a lower electron transfer rate is expected and, consequently, the slowest overall transfer kinetics among all the complexes.

Finally, the potential effect of the supporting electrolyte was evaluated, as the coordination sphere of the complex might be altered. Fig. 7 shows cyclic voltammograms for complex **1** in 0.1 M NaCl or 0.1 M KNO_3. With the second electrolyte, the intensity is halved, and the irreversibility of the process is intensified, as is evidenced by the almost complete disappearance of the oxidation peak at 100 mV s^{-1}. The same trend is observed for complex **2** (see Fig. S10). Electrolytes containing large ions may hinder the interaction between the redox species and the electrode, affecting its electrochemical behavior. At the same time, Cl^- is a more nucleophilic and coordinating ion than NO_3^-, meaning it can form more stable complexes affecting their availability for electron transfer. On those bases, the evaluated complexes are more stable and

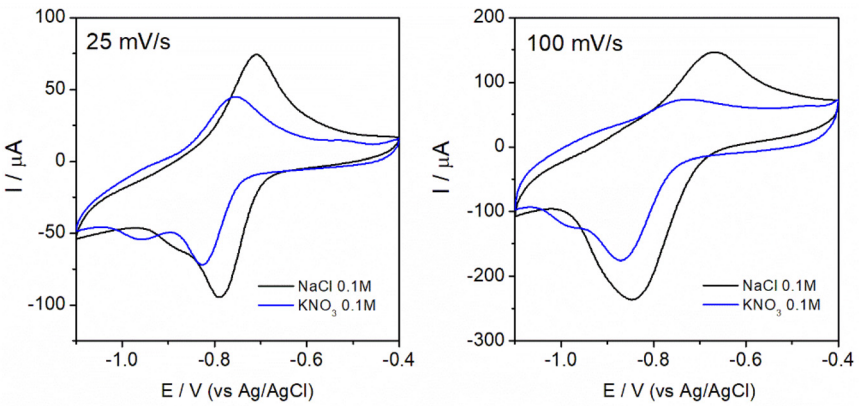

Fig. 7 Cyclic voltammograms of complex **1** (potential range −1.1 to −0.4 V) in 0.1 M NaCl (black) and 0.1 M KNO_3 (blue) at (left) 25 mV s^{-1} and (right) 100 mV s^{-1}.

exhibit better electrochemical properties dissolved in 0.1 M NaCl.

Interaction of Ru complexes with BSA

The study of the interaction of ruthenium complexes **1–3** with bovine serum albumin (BSA) has been carried out through fluorescence, circular dichroism (CD), dynamic light scattering (DLS) and zeta potential experiments.

Fluorescence quenching. The analysis of changes in BSA intrinsic fluorescence upon interaction with **1–3** provided insights into the extent of complex–protein interactions. BSA is a highly soluble and stable protein that has a high affinity for a variety of ligands and is widely used in studies of protein-compound interactions.[28] BSA has three helical domains (I–III), each divided on two sub-domains (A–B), with two tryptophan (Trp) residues (Trp134 and Trp213).[29]

The intrinsic fluorescence of tryptophan can be measured using fluorescence spectroscopy, and the quenching of its intensity upon addition of a test complex can provide information about the nature of the protein–ligand interaction. Affinity of the compound to a protein can be described by two main binding parameters: static and dynamic. Static quenching occurs when fluorophore and quencher form a complex in the ground state, while dynamic is related to collision of these two molecules, resulting in the fluorophore fluorescence recovery.[30] Since the bimolecular quenching constant k_q of approximately 1×10^{10} M^{-1} s^{-1} represents the upper limit for diffusion-controlled quenching in aqueous media and the average lifetime of biomolecules in the absence of a quencher is around 10^{-8} s, the corresponding Stern–Volmer constant K_{sv} for dynamic quenching is roughly 100 M^{-1}.[31,32] Binding mechanism can be assessed by calculating Stern–Volmer constant, using the equation:

$$\frac{F_0}{F} = K_{sv}[Q] + 1 = k_q\tau_0[Q] + 1$$

where: F_0 is fluorescence of fluorophore in the absence of the quencher, F is fluorophore fluorescence with the quencher, K_{sv} is the Stern–Volmer constant, Q is concentration of the quencher, k_q is biomolecular quenching constant and τ_0 is an average lifetime of the fluorophore (6×10^{-9} s for BSA). BSA fluorescence emission was measured at 345 nm, and changes in intensity upon complex addition were analyzed to determine the binding mechanism (Fig. 8). Based on k_q values, it was stated that all tested complexes bond to BSA *via* static mechanism and complex **2** presented the highest affinity toward the protein ($K_{sv} > 10^4$) (see Table S1 and Fig. S11). Binding constant (K_b) describes the force of binding between the protein and the ligand and can be determined by the spectroscopic analysis. Binding with BSA was the strongest in the case of complex **2** with $\log K_b$ value 4.7 ± 1.6 (see Table S1). Complex **1** required substantially higher concentrations to produce measurable fluorescence changes, whereas complexes **2** and **3** quenched BSA fluorescence already at lower concentrations. This observation indicates that complex **1** has a lower effective affinity for BSA. The result is consistent with a model in which a shorter PEG environment limits efficient approach of the metal core to protein fluorophores, reducing quenching efficiency. Moreover, no visible aggregation of compound **1** was detected under the experimental conditions (see DLS data below). Therefore, the need for higher concentrations likely reflects genuinely weaker binding rather than an artefact.

However, downward curvatures obtained in Stern–Volmer calculations (see Fig. S11) suggested that accessibility of the tryptophan residues in BSA may differ, and this is why a modified equation was applied:

$$\frac{F_0}{F_0 - F} = \frac{1}{f_a K_a[Q]} + 1/f_a$$

where: F_0 is fluorescence of fluorophore in the absence of the quencher, F is fluorophore fluorescence with the quencher, Q is concentration of the quencher, f_a is accessible fraction and K_a is the Stern–Volmer constant of the accessible fraction. These parameters were obtained in least-squares method using nonlinear fit. Results presented in Table 4 indicate that mechanism of binding for all tested complexes is static. Although complex **1** exhibits the weakest binding to BSA compared to complexes **2** and **3**, its f_a value of 1.099 suggests the presence of a single, specific binding site. On contrary, binding between BSA and complexes **2** and **3** was relatively strong, proving their high affinity to BSA, despite their lower f_a values (0.65 and 0.59, respectively) indicating a few, non-specific binding sites on protein. Obtained results are well aligned with other ruthenium complexes described in literature, where static binding mechanism was also confirmed.[33,34]

Circular dichroism. Measuring spectra in far-UV wavelengths (195–260 nm) is a standard practice of visualizing secondary structure of the protein. Analyzing spectra alteration upon addition of complexes **1–3** can provide information about changes in α-helix and β-sheets structures and subsequently, functionality of the protein and toxicity. Alpha-helical structure of proteins is observed by two characteristic negative bands at 208 nm and 220 nm.[35] Considering specific binding kinetics for each complex, as proved by quenching analysis, different BSA : ruthenium complexes molar ratios were used to perform CD experiment (Fig. 9). Although the highest affinity to BSA was stated for complex **2**, change in α-helix structure was observed at the same level for complexes **2** and **3** and not far from complex **1**. Although these alterations were still minor and not statistically significant, the CD spectra indicate subtle yet distinct differences in the interaction of BSA with each Ru–PEG complex. For complex **1**, the spectra almost completely overlap with native BSA, suggesting negligible conformational changes. In contrast, complex **2** shows slight alterations in ellipticity near 230 nm, consistent with minor perturbations in the α-helical domains. Complex **3** produces the most pronounced effect, with decreased signal intensity at ~210 nm and ~230 nm, indicating partial unfolding or loosening of the secondary structure. These findings suggest that, although the differences are very subtle, each complex interacts with BSA through distinct binding modes or affinities, leading to different degrees of structural rearrangements. Consequently,

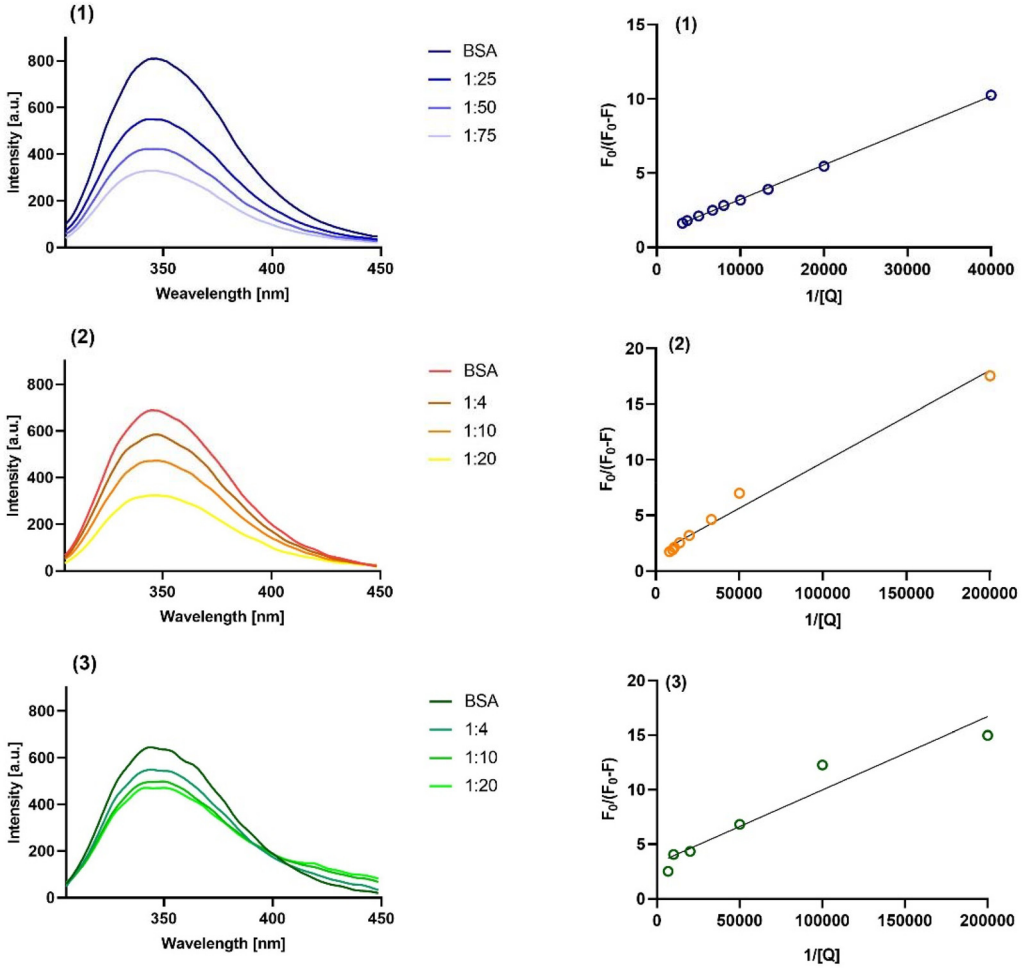

Fig. 8 (Left) Changes in tryptophan fluorescence intensity spectra after addition of complexes **1–3** respectively. (Right) Plots of modified Stern–Volmer. All measurements were conducted in phosphate buffer, 10 mmol L^{-1}, concentration of BSA, 5 μmol L^{-1}. Graphs represent mean, n = 3.

Table 4 Stern–Volmer of accessible fraction (K_a)[a] and fraction accessible to the quencher (f_a)[a] describing BSA-complexes interactions at 21 °C in phosphate buffer (10 mM L^{-1}, pH = 7.4)

Complex	$K_a/(M^{-1})$	f_a	R^2
1	4.55×10^3	1.099	0.999
2	1.91×10^4	0.65	0.986
3	1.71×10^4	0.59	0.989

[a] The association constants (K_a) and accessible fractions (f_a) were calculated using averaged fluorescence data obtained from three independent measurements. Since the modified Stern–Volmer model is non-linear and the fitting was performed on averaged values rather than on individual replicates, the standard deviations of K_a and f_a could not be reliably determined.

the percentage content of β-sheets and random coils in the protein structure did not change considerably after the addition of the tested complexes. Fears *et al.* proved that protein (BSA) denaturation caused helical level decline to 30%.[36] Comparing these results to those obtained for ruthenium dendrimers, it was observed that ruthenium complexes (**1–3**) alter secondary structure of albumin to a lesser degree and thus they could be excluded as a possible cause of protein degradation.[37]

DLS and zeta potential. Interactions between proteins and complexes **1–3** can be also described by changes in a protein surface charge and hydrodynamic diameter. In physiological pH (~7.4) albumin size oscillates around 10 nm and has negative charge.[38] However proteins are large and complex molecules, prone to clump and aggregate, and this is visible through high polydispersity index (PDI) by DLS measurements (see Fig. S12–S14). This aggregation may be caused by high charge distribution, and the effect is difficult to diminish.[39] Nevertheless, some changes after addition of the ruthenium complexes were observed. As expected, the hydrodynamic diameter of BSA when interacting with **2** or **3** slightly increased, however these changes were insignificant. Due to high polydispersity of tested samples observed as PDI values above 0.5, it was impossible to analyze higher concentration of the complexes. In the case of complex **1**, size of BSA-complex aggregate decreased with rising concentration of the complex and simultaneously PDI sustained at low level, suggesting that samples

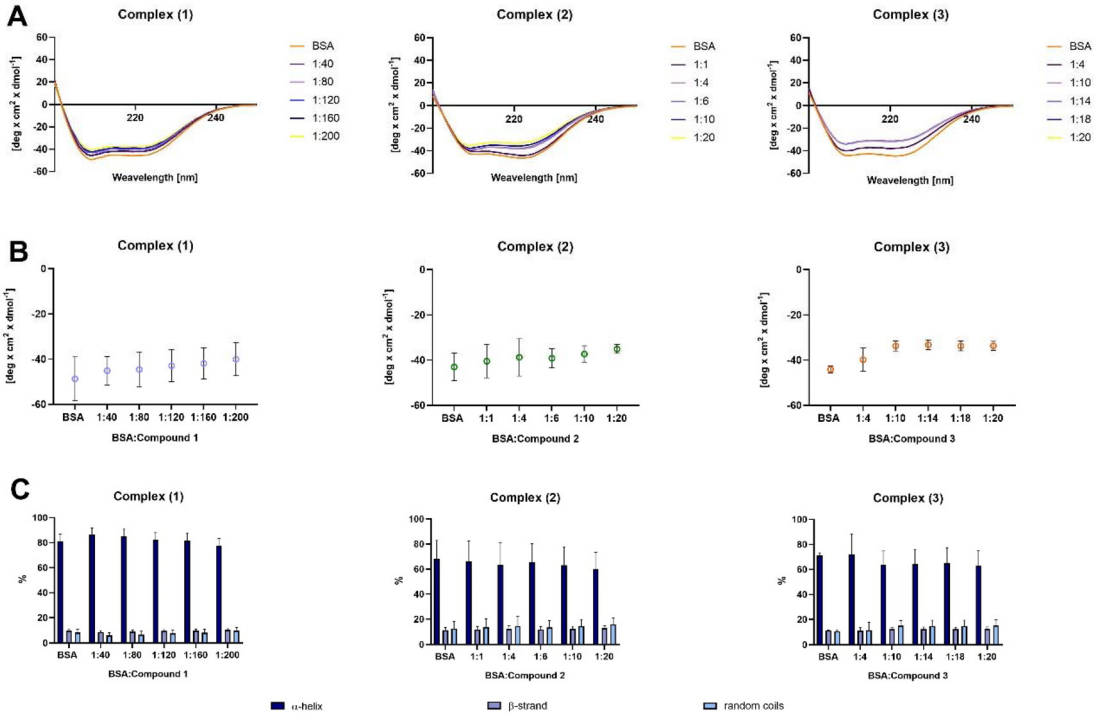

Fig. 9 (A) CD spectra of BSA upon addition of tested complexes **1–3**. (B) Ellipticity of BSA in the presence of the complexes at λ = 208 nm. (C) Contribution of α-helix, β-strand, and random coils conformation to the overall structure of the albumin calculated with CDNN Software. Graphs show mean ± SD, n = 3.

were monodispersed. Alhazmi *et al.* observed similar effect explaining smaller size of BSA after addition of Cu(II) ions by the fact that binding sites of the BSA were saturated by cations which kept exterior surface of protein hydrophilic, hindering formation of protein aggregates.[40] At the same time, zeta potential measurements indicated that BSA with complex **1** had more negative charge than BSA alone. This effect was not observed for other tested complexes and increasing concentrations of complexes **2** and **3** did not change the negative surface charge of albumin. The different behavior observed may be due to the chemical and biophysical properties that these complexes induce. Beside the capacity of complex **1** to reduce the aggregation and therefore to increase the exposition of negative charged group to the exterior, the Ru–Cl bond within the complexes is weak and can be easily broken, releasing Cl^- ions that may have an affinity for specific binding sites on BSA, thereby increasing the ζ-potential, as observed for complex **1**. However, these effects could be attenuated when large PEG chains are present, as in complexes **2** and **3**. A high ζ-potential (>+30 mV or <−30 mV) is indicative of low aggregation potential, whereas values closer to zero correspond to higher aggregation possibilities.[41] This could explain the polydispersity observed in the tested protein–complex association.

Cancer cell cytotoxicity

Based on MTT technique, cytotoxicity studies were conducted in human liver (HepG2 and HuH7) and prostate (PC3 and LNCaP) derived cancer cell lines. The cytotoxicity of complexes **2** and **3**, as well as the ligand precursors **L7** and **L8**, was evaluated and compared with the data previously reported for complex **1** and its precursor **L2**.[15] None of them were toxic up to 100 μM in any of the cell lines used, except for complex **3** that exceptionally showed hepatocellular specific toxicity over 50 μM dose (see Fig. 10 and Fig. S15).

Also, cytotoxicity was conducted for complexes **1–3** on PNT2 cell line, derived from normal human prostate epithelium which is widely used as a non-tumorigenic control model. The study showed no toxicity up to 100 μM (see section S11, Fig. S16). These results highlight the importance of tailoring PEG chain length not only to improve solubility and stability but also to ensure efficient cellular uptake in target tissues, particularly when designing metal-based chemotherapeutic agents. The presence of PEG_{2000} in the metal complex appears to influence cytotoxicity in a cell line–dependent manner. The complex exhibited significant activity in HepG2 and HuH7 cells at higher concentrations but was totally inactive in PC3 and LNCaP cells, suggesting that the PEG chain length may selectively affect cellular uptake and/or intracellular processing. Cells derived from hepatic tissue, are characterized by high metabolic and endocytic activity, as well as the expression of various membrane transporters, which may facilitate the uptake of moderately PEGylated complexes, leading to greater intracellular accumulation and cytotoxicity. Short and medium PEG chains may not significantly alter pharmacokinetics or uptake pathways, limiting their activity even at high doses. Long PEG (PEG_{2000}), despite being a barrier at low concen-

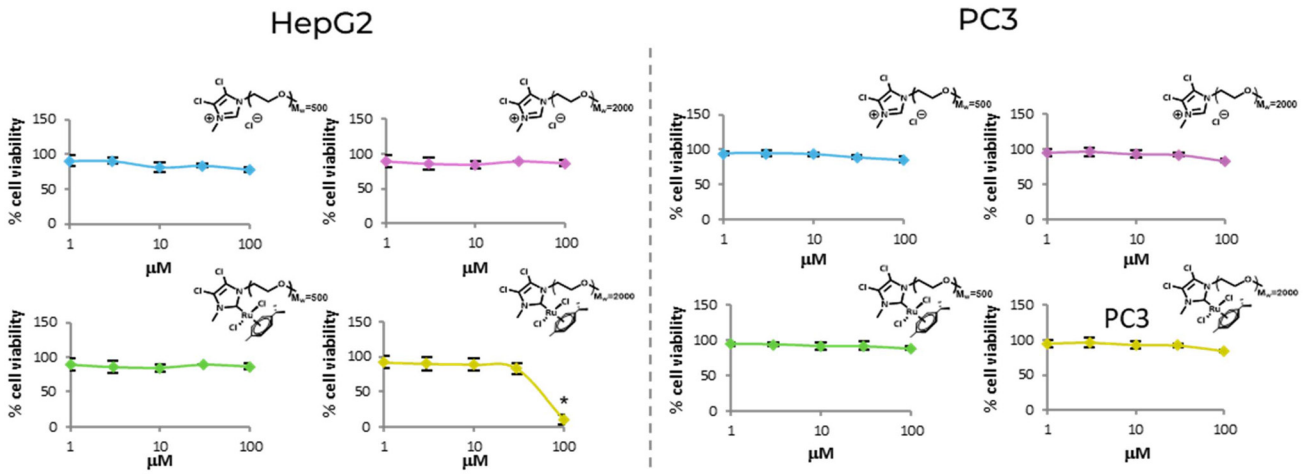

Fig. 10 Cell viability data measured by the MTT assay for complexes **2** and **3** and their respective precursor ligands **L7** and **L8** in HepG2 and PC3 cell lines. For HuH7 and LNCaP see Fig. S15. Standards anticancer drugs in these cell lines cisplatin (3.9–93 mM) or docetaxel (0.2 mM–3.0 mM) IC_{50} values recorded from literature (see section S12 in the SI). Measurements were performed by three independent experiments, each performed in duplicate and using separately synthesized vials.

trations, enables alternative uptake and trafficking mechanisms only when present in high enough concentrations, by enhancing stability and prolonging extracellular presence along with triggering of alternative uptake pathways at high dose. Polyethylene glycol (PEG) is primarily metabolized in the liver, where its biotransformation involves sequential oxidative steps catalyzed by alcohol dehydrogenase (ADH) and aldehyde dehydrogenase, both of which are abundantly expressed in hepatocytes.[42,43] Additional enzymatic pathways, including cytochrome P450 isoforms and sulfur transferases, also contribute to PEG metabolism in hepatic tissue. By contrast, prostate cancer cells exhibit reduced expression of metabolic enzymes, together with a more rigid plasma membrane architecture and diminished endocytic capacity, which collectively limit the internalization of sterically bulky PEG2000-conjugated complexes. These findings highlight the critical importance of optimizing PEG chain length to balance metabolic stability, hepatocellular safety, and efficient cellular uptake in a tumor-specific context.

Transfer hydrogenation reactions

Ruthenium–NHC complexes are known to be efficient catalysts for transfer hydrogenation (TH) reactions.[24] The catalytic activities of complexes **1–3** were tested for TH of ketones using cyclohexanone as model substrate. The standard experiment was carried out in different conditions of hydride sources and solvents with a Ru loading of 1 mol% and the results are summarized in Table 5. The reaction profiles obtained for the three complexes show that cyclohexanone is reduced to cyclohexanol at 80 °C in 100% yield within 0.5 h using KOH/^{i}PrOH as hydride source (TOF: 20 h^{-1} under these conditions). These activities are similar to those measured for analogous Ru–NHC complexes.[24,44] When cyclohexanone was reduced using sodium formate in water at 80 °C, 100% conversions were obtained after 24 h for the three complexes, according to a lower strength of the base used. However, differences in the reaction profiles were observed at 6 h, although a systematic relationship with the size of the PEG cannot be observed. No

Table 5 Transfer hydrogenation reactions of cyclohexanone or NAD^+ with complexes **1–3** [a]

Complex	Hydride source	Substrate	Solvent	T (°C)	Conversion[b](%)	Time (h)	TON (time, h)	TOF (h^{-1})
1	KOH/^{i}PrOH	Cyclohexanone	^{i}PrOH	80	100	0.5	10	20
1	Formate	Cyclohexanone	D_2O	80	96	24		
1	Formate	Cyclohexanone	D_2O	80	63	6	6.3	1.05
1	Formate	NAD^+	D_2O	25	61	24	6.1	0.25
2	KOH/^{i}PrOH	Cyclohexanone	^{i}PrOH	80	100	0.5	10	20
2	Formate	Cyclohexanone	D_2O	80	100	24		
2	Formate	Cyclohexanone	D_2O	80	75	6	7.5	1.25
2	Formate	NAD^+	D_2O	25	43	24	4.3	0.17
3	KOH/^{i}PrOH	Cyclohexanone	^{i}PrOH	80	100	0.5	10	20
3	Formate	Cyclohexanone	D_2O	80	100	24		
3	Formate	Cyclohexanone	D_2O	80	56	6	5.6	0.94
3	Formate	NAD^+	D_2O	25	23	24	2.3	0.10

[a] Catalyst/base/substrate: 1/50/10. [b] Conversions were determined by ^{1}H-NMR.

conversions were found when the chemical processes were conducted at room temperature.

After demonstrating efficient catalytic activity both in the classical isopropanol/KOH system and formate in water as hydride sources, a natural next step is to transfer this reactivity to the co-enzyme nicotinamide adenine dinucleotide (NAD^+) as substrate (see Table 5). The Ru–NHC complexes **1–3** bearing PEG chains of increasing length display a clear decrease in catalytic activity for the hydrogen transfer reaction from NAD^+ to NADH, with conversion (TOF) values of 61% (0.25 h^{-1}), 43% (0.17 h^{-1}), and 23% (0.10 h^{-1}), respectively. This trend can be primarily attributed to steric effects: as the PEG chain length increases, the steric bulk around the metal center becomes more pronounced, hindering the approach of the NAD^+ substrate to the active site and thereby reducing the efficiency of hydrogen transfer, further limiting the overall catalytic performance, in agreement with the CV data. The observed TOF values are relatively modest compared to related Ru–NHC complexes reported in the literature for transfer hydrogenation reactions involving NAD^+ or similar substrates.[45,46] Interestingly, when the Me group on the NHC ligand in complex **1** was replaced by a more lipophilic substituent, $-(CH_2)_4SiEt_3$, the resulting complex [$RuCl_2(\eta^6$-*p*-cymene)(triethylsilylbutyl–NHC–PEG147)] (**4**), previously reported elsewhere,[15] displayed lower conversion values (TOF ≈ 35%, 0.15 h^{-1}) (see Fig. S16). This complex also exhibited cytotoxic activity, with IC_{50} values of 4.75 μM in a hepatic cancer cell line and 8.50 μM in a prostate cancer cell line. This would mean that the increase in lipophilicity would generate more cytotoxic systems but with lower catalytic capacity.

To overcome the observed moderate intrinsic activity of the PEGylated systems, different delivery platforms were employed using complex **2** as proof of concept: dendritic micelles (one cationic and one anionic) previously developed by our research group,[47] as well as BSA. In this regard, confined spaces have been exploited in catalysis to perform reactions that are otherwise not feasible in bulk solution or to significantly improve catalytic activity.[48,49] The addition of micelles or protein carriers such as BSA can provide significant benefits in pure water by offering (i) a confined microenvironment that pre-organizes the NAD^+ substrate around the metal center, acting as a nanoreactor, increasing the frequency of effective collisions and overall catalytic efficiency and (ii) protection of the metal complex from deactivation pathways (*e.g.*, hydrolysis or unwanted side reactions) and facilitate better dispersion and stability under purely aqueous conditions. These approaches could help overcome the observed moderate intrinsic activity of the PEGylated systems (Fig. 11).

Regarding the use of dendritic micelles, the catalytic activity is significantly higher in cationic micelles (70–80% conversion) compared to anionic ones (15% conversion) after 24 h of reaction. Therefore, the cationic micellar system loaded with complex **2** nearly doubles its efficacy compared to complex **2** alone (40% conversion). The fact that these Ru complexes generate cationic species in water[15] could explain this difference in behavior. In the case of cationic micelles, the complex is partially embedded within the micellar structure, whereas with anionic micelles, the electrostatic interaction is mainly superficial. When using BSA as a carrier, two ratios (4 : 1 and 1 : 1) for the system complex **2** : BSA were tested, while keeping the final Ru concentration constant. A higher catalytic activity was observed after 24 hours at the higher 4 : 1 ratio. This suggests that at lower metal-to-protein ratios, the metal center may preferentially occupy deeper, less accessible binding sites within BSA, limiting its availability for reaction. In contrast, when excess metal is present (4 : 1), the internal sites become saturated and additional metal centers can bind to more accessible, superficial regions of the protein, thus enhancing the overall reactivity. Although this hypothesis remains tentative, it highlights the potential importance of site accessibility and binding dynamics in modulating the catalytic behavior of BSA–metal complexes. In addition, the 1 : 1 ratio showed a distinct induction period of approximately 6 hours, during which virtually no product formation was detected. This suggests that BSA may initially sequester the metal center within less accessible internal sites, effectively protecting it from premature side reactions or degradation. Notably, once this induction phase ends, the reaction proceeds

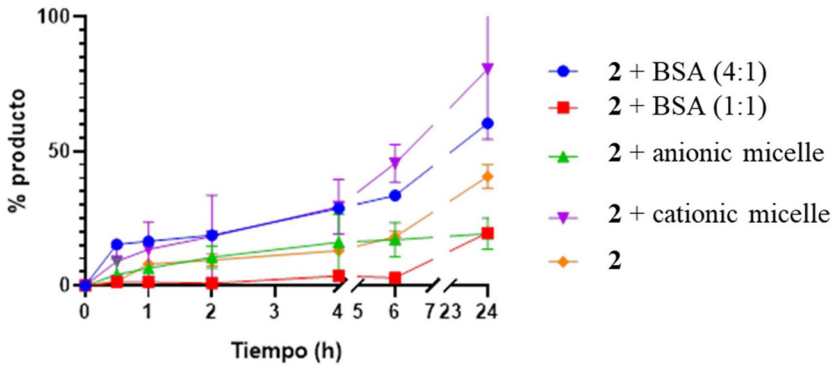

Fig. 11 Transfer hydrogenation reaction profiles of complex **2** in the presence of dendritic micelles or BSA as carriers for the conversion of NAD^+ to NADH in D_2O at room temperature, using a catalyst : HCOONa : substrate ratio of 1 : 50 : 10.

with a slope comparable to that observed for the 4 : 1 system, indicating that the intrinsic reactivity of the released active center is similar under both conditions. This tentative finding supports the hypothesis that BSA may act not only as a solubilizing and transport agent, but also as a temporal protective host, delaying activation until cellular uptake occurs and thus potentially enhancing selectivity and stability in biological environments. Nevertheless, further studies will be necessary to support this hypothesis and confirm its relevance under biological conditions.

Conclusions

Ruthenium complexes containing PEG-type substituents with different chain lengths were successfully synthesized and characterized. The PEG fragment strongly influences their reactivity by modulating the approach to biomolecules and slowing down chemical processes. Although their reduction potentials are identical, the kinetics are governed by PEG size: larger PEG units impose greater steric hindrance around the metal center, leading to slower mass transport to the electrode and hampering heterogeneous electron transfer. Consequently, reduction processes, hydride formation, and substrate binding become progressively hindered with increasing PEG length. Furthermore, the composition of the medium affects the stability of the reduced species.

The interaction of these systems with BSA confirmed a predominantly static quenching mechanism, indicative of complex formation between the protein and the Ru complex. However, in the presence of sufficiently large PEG units, a dynamic contribution is also observed. This mechanism suggests that BSA can act as a potential carrier, facilitating compound transport. Short PEG fragments tend to form more discrete conjugates, whereas longer PEG units promote stronger interactions. Importantly, all systems proved to be generally non-toxic.

Finally, the Ru–NHC–PEG complexes were able to function as catalytic agents in hydrogen transfer processes, including the reduction of ketones or NAD^+. Their activity is enhanced when using carriers such as cationic micelles or BSA. Taken together, these results demonstrate that non-toxic Ru–PEG systems may serve as promising candidates for catalytic applications within biological environments. Increasing PEG length enhances solubility, stability, and biocompatibility, but excessive PEG can sterically shield the metal center and reduce catalytic accessibility. In our series, the intermediate PEG length (complex **2**), provides the best balance between hydrophilicity and catalytic efficiency.

The Ru–NHC–PEG complexes are reasonably non-toxic, stable, and soluble, and exhibit hydrogen transfer activity. In this sense, they could be explored as intracellular catalysts, particularly for bioorthogonal or therapeutic applications (*e.g.*, cofactor regeneration, prodrug activation). In addition, the formation of stable adducts with BSA, together with their enhanced catalytic activity in TH, opens new avenues for their application as artificial metalloenzymes within cells. Future works are in progress in this direction.

Experimental sections

For general procedures and data characterization of PEG-substituted imidazole and imidazolium ligands and standard protocols for transfer hydrogenation reactions and cancer cell toxicity essays, see SI.

General procedure for the formation of ruthenium NHCs complexes

Ruthenium complexes synthesis was initiated by dissolving the corresponding imidazolium salts in dichloromethane (DCM) into a volumetric flask in imperial topaz-colored glass so that to impede possible silver deposition. Afterwards, silver (I) oxide (0.6 equiv.) was introduced into the flask and the mixture was stirred overnight at room temperature. The following day, completion of the reaction was checked by ^{1}H-NMR since the disappearance of the acidic proton confirms the carbene formation. Next, the mixture was filtered with a syringe filter for silver salts withdrawal to a volumetric flask in imperial topaz-colored glass. Dichloro(*p*-cymene)ruthenium(II) dimer (0.45 equiv.) was then introduced into the flask, and the resulting mixture was stirred at room temperature overnight. Completion of the reaction was checked by ^{1}H-NMR. Finally, the corresponding ruthenium complex was purified by silica column chromatography with DCM/MeOH (27/1).

Synthesis of $[RuCl_2(\eta^6\text{-}p\text{-cymene})(Me\text{–}NHC\text{–}PEG_{500})]$ (2). Complex **2** was synthesized following the general procedure aforementioned. Compound **L7** (223.8 mg, 0.3 mmol, 1 equiv.); Ag_2O (42.6, 0.2 mmol, 0.6 equiv.); $[RuCl_2(\eta^6\text{-}p\text{-cymene})]_2$ (75.1 mg, 0.1 mmol, 0.4 equiv.); complex **2** afforded (88.3 mg, 28.8% yield). ^{1}H NMR (400 MHz, $CDCl_3$) δ 5.52 (m, 5H, 4$(CH)_{pcym}$ + $(CH)_{PEG500\ diast.}$), 4.27 (s_{broad}, 1H, $(CH)_{PEG500\ diast.}$), 4.01 (s, 3H, $CH_{3\ Me\text{-}Imid}$), 3.97–3.49 (m, $(CH_2)n_{\ PEG500}$), 3.38 (s, 3H, $CH_{3\ OMe}$), 2.99 (p, J = 6.9 Hz, 1H, $CH_{isoprop.\text{-}pcym}$), 2.10 (s, 3H, $CH_{3\ Me\text{-}pcym}$), 1.30 (d, J = 6.9 Hz, 6H, $(CH_3)_{2\ isoprop.\text{-}pcym}$) ppm. ^{13}C NMR (101 MHz, $CDCl_3$): δ 178.7 ($C_{Imid\text{-}2'}$), 119.0 ($C_{Imid\text{-}4'}$), 117.1 ($C_{Imid\text{-}5'}$), 109.4 ($C_{ipso\ pcym.}$), 99.0 ($C_{ipso\ pcym.}$), 86.9 ($CH_{pcym.}$), 85.6 ($CH_{pcym.}$), 83.7 ($CH_{pcym.}$), 82.3 ($CH_{pcym.}$), 72.0 ($(CH_2)n_{\ PEG500}$), 70.6 ($(CH_2)n_{\ PEG500}$), 70.6 ($(CH_2)n_{\ PEG500}$), 70.5 ($(CH_2)n_{\ PEG500}$), 70.4 ($(CH_2)n_{\ PEG500}$), 69.1 ($(CH_2)n_{\ PEG500}$), 59.1 ($CH_{3\ OMe}$), 51.4 ($CH_{2\ PEG500\ diast.}$), 38.7 ($CH_{3\ Me\text{-}Imid}$), 30.9 ($CH_{isoprop.\text{-}pcym}$), 23.6 ($(CH_3)_{2\ isoprop.\text{-}pcym}$), 21.7 ($(CH_3)_{2\ isoprop.\text{-}pcym}$), 18.9 ($CH_{3\ Me\text{-}pcym}$). MS-ESI-TOF MS: the peaks corresponding to $[M - Cl]^+$, $\{[(cymene)ClRu]\text{-}(CH_2CH_2O)_nMe\}^+$: n = 11, MW = 920 Da; n = 12, MW = 963 Da. The more intense peak corresponds to n = 10 and 11.

Synthesis of $[RuCl_2(\eta^6\text{-}p\text{-cymene})(Me\text{–}NHC\text{–}PEG_{2000})]$ (3). Complex **3** was synthesized following the general procedure aforementioned. Compound **L8** (228.3 mg, 0.1 mmol, 1 equiv.); Ag_2O (14.5 mg, 0.06 mmol, 0.6 equiv.); $[RuCl_2(\eta^6\text{-}p\text{-cymene})]_2$ (25.6 mg, 0.04 mmol, 0.4 equiv.); complex **3** afforded (192.6 mg, 75.1% yield). ^{1}H NMR (400 MHz, $CDCl_3$) δ

5.26 (m, 5H, $(CH)_{4\ pcym.}$ + $(CH_{2\ PEG2000})_{diast.}$), 4.22 ($s_{broad}$, 1H, $(CH_{2\ PEG200})_{diast.}$), 3.94 (s, 3H, s, 3H, $CH_{3\ Me\text{-}Imid}$), 3.58 (m, $(CH_{2\ PEG2000})_n$), 3.31 (s, 3H, $CH_{3\ OMe}$), 2.92 (p, J = 6.9 Hz, 1H, $CH_{isoprop.\text{-}pcym}$), 2.04 (s, 3H, $CH_{3\ Me\text{-}pcym}$), 1.24 (d, J = 6.9 Hz, 6H, $(CH_3)_{2\ isoprop.\text{-}pcym}$). ^{13}C NMR (101 MHz, $CDCl_3$): δ 178.8 ($C_{Imid\text{-}2'}$), 118.9 ($C_{Imid\text{-}4'}$), 117.05 ($C_{Imid\text{-}5'}$), 109.4 ($C_{ipso\ pcym.}$), 99.0 ($C_{ipso\ pcym.}$), 86.8 ($CH_{pcym.}$), 85.4 ($CH_{pcym.}$), 83.6 ($CH_{pcym.}$), 82.2 ($CH_{pcym.}$), 72.0 ($(CH_2)_{n\ PEG500}$), 70.4 ($(CH_2)_{n\ PEG500}$), 69.11 ($(CH_2)_{n\ PEG500}$), 59.1 ($CH_{3\ OMe}$), 51.4 ($CH_{2\ PEG500\ diast.}$), 38.7 ($CH_{3\ Me\text{-}Imid}$), 30.8 ($CH_{isoprop.\text{-}pcym}$), 18.8 ($(CH_3)_{2\ fisoprop.\text{-}pcym}$), 18.5 ($CH_{3\ Me\text{-}pcym}$). MS-ESI-TOF MS: not accurate data were obtained due to large molecular weight and polydispersity of the PEG fragment.

Molecular modelling

3D computer models of Ru–PEG complexes were constructed using the Dendrimer Builder as implemented in the Materials Studio software package from BIOVIA (formerly Accelrys, v. 8.0). The same software was employed for parameterization and all subsequent simulation steps, *i.e.*, the Forcite module (parameterization, simulations, and analyses) and the Amorphous Cell module for creation of the solvated systems. The Universal forcefield[50] was used for parameterization of all Ru–PEG structures, partial charges were calculated using QEq method.[51] SPC/E water model[52] was used for simulations in explicit solvent. To allow simultaneous simulations of Ru–PEG complex and SPC/E water, the relevant water atom types (OW, HW) were added to the UFF parameter file, along with all relevant SPC/E parameters. The rigidity of the water model during molecular dynamics was ensured by constraining the OW–HW and HW–HW distances using measurement constraints (distance measurement objects that can be fixed). During the geometry optimization of solvated systems (potential energy minimization), water molecules rigidity was maintained by explicitly treating them as rigid motion groups (see the option "keep motion groups rigid"). The neutrality of solvated systems was ensured by adding one Cl^- anion into simulation box, since the Ru atom coordinates one H_2O molecule in water, resulting in the Ru–PEG complex acquiring a +1 charge ($1|e|$). 3500 H_2O molecules were used for simulation of each Ru–PEG complex. The length of each Molecular Dynamics simulation in explicit solvent was 1.5 ns (1 500 000 1 fs time steps). Simulations were done at constant temperature and pressure (T = 298 K, P = 10^5 Pa). Temperature was regulated using a Nosé thermostat (Q ratio: 0.01), and pressure was controlled with an Andersen barostat (cell time constant: 1 ps).[53,54] Electrostatic interactions were calculated using the classical Ewald summation method with an accuracy of 1×10^{-5} kcal mol^{-1} and a buffer width of 0.5 Å. van der Waals interactions were evaluated using an atom-based summation method with a cubic spline truncation at 16 Å, a spline width of 1 Å, long-range correction enabled, and a buffer width of 0.5 Å. Before simulations in solvent Ru–PEG complexes were simulated in vacuum at temperature 298 K, for 2 ns (2 000 000 1 fs time steps), to obtain suitable starting configurations for simulations in water. In this case the electrostatic and van der Waals interactions were both calculated using an atom-based summation method with a cubic spline truncation at a cutoff distance of 60 Å (spline width 1 Å, buffer width 0.5 Å). For structural analyses (RDF, R_g) the last 0.5 ns of the MD trajectories from simulations in solvent were used. UCSF Chimera software was used for all visualizations.[55]

Fluorescence quenching

Complex-induced quenching of intrinsic Trp fluorescence in BSA provided information of character of the interaction between studied ruthenium complexes and protein. BSA solution in a concentration 5 μmol L^{-1} in 10 mmol L^{-1} phosphate buffer, pH-7.4 was titrated with tested complexes and measured on PerkinElmer LS-50B spectrofluorometer (UK). Fluorescence spectra were observed at wavelength emission range 305–445 nm (excitation: λ = 295 nm). Excitation and emission slits were set for 2.5 nm and 10 nm, respectively.

Circular dichroism

Analysis of bovine serum albumin (BSA) secondary structure alterations upon addition of tested complexes was performed by circular dichroism technique. The protein solution at final concentration 0.5 μmol L^{-1} in 10 mmol L^{-1} phosphate buffer, pH-7.4 was titrated with increasing amount of each complex and measured with Jasco J-815 CD spectrometer (Jasco International Co., Ltd, Tokyo, Japan) in 0.5 cm quartz cell. CD spectra were observed at 195–260 nm wavelengths. The protein secondary structure and distribution of α-structure and β-sheet percentage under the influence of ruthenium complexes were calculated using the CDNN software available at: https://cdnn-circular-dichroism-spectroscopy-deconvolution.updatestar.com.

DLS and zeta potential

BSA hydrodynamic diameter and zeta potential changes after addition of tested complexes were measured on Malvern Zetasizer Nano ZS (UK). Pure protein solution at 0.25 μmol L^{-1} in 10 mmol L^{-1} phosphate buffer, pH-7.4 was treated with increasing amounts of the complexes. Dynamic light scattering (DLS) measurements were used to provide information about alteration in protein size. Measurements were performed in triplicate, with five runs per measurement. Zeta potential showed changes in the surface charge of the protein. Zeta potential was measured in triplicate, with seven runs per measurement and calculated with the Helmholtz–Smoluchowski's equation.

Author contributions

O. B. synthesized the compounds and contributed to the biomedical experiments. T. R.-P. performed the catalytic experiments. A. B. carried out the cytotoxicity assays. M. M. performed the molecular modelling. M. C. conducted the electrochemical characterization. E. O. and M. I. carried out biophysical experiments. J. C. provided expertise on molecular

homogeneous catalysis and supervised the experiments. R. G., I. D. L., M. B., and J. C. checked the data and wrote the manuscript. R. G., I. D. L., J. C., A. E., M. M., and M. C. provided funding. All authors proofread the manuscript and approved the final version.

Conflicts of interest

The authors declare no conflict of interest.

Data availability

Data supporting this study are contained in the manuscript and supplementary information (SI). Supplementary information (SI) is available. See DOI: https://doi.org/10.1039/d5dt02391b.

Acknowledgements

M.M. acknowledge the assistance provided by the Research Infrastructure NanoEnviCz (no. LM2023066) and the project Pro-NanoEnviCz (Reg. No. CZ.02.1.01/0.0/0.0/16_013/0001821), supported by the Ministry of Education, Youth and Sports of the Czech Republic, and the European Union-European Structural and Investments Funds in the frame of the Operational Programme Research Development and Education. ERDF/ESF (project "UniQSurf – Centre of Biointerfaces and Hybrid Functional Materials" No. CZ.02.1.01/0.0/0.0/17_048/0007411). This work has also been supported by the University of Alcalá through the projects GP2024-02 (RG) and GP2024-03 (IDL), and the ISCIII through the project FORT23/00046, Program FORTALECE of the Ministerio de Ciencia e Innovación y Universidades of Spain (RG). This work was also supported by the Spanish Ministry of Science, Innovation and Universities (Grant PID2020-118154GB-I00 (A.E.), and Grant PID2023-152298NB-I00 (A.E.), TED2021132720B-I00) (A.E.), JDC2022048210-I Juan de la Cierva fellowship program (M.C.); and by the Community of Madrid (Grant CM/JIN/2021-012) (A.E.) and Y2020/NMT6312 (NEURO–CHIPCM) (A.E., M.C.).

References

1 D. Fan, Y. Cao, M. Cao, Y. Wang, Y. Cao and T. Gong, Nanomedicine in cancer therapy, *Signal Transduction Targeted Ther.*, 2023, **8**, 293.
2 O. Sun, X. Sun, X. Ma, Z. Zhou, E. Jin, Y. Shen, E. A. van Kirk, W. J. Murdoch, J. R. Lott, T. P. Lodge, M. Radosz and Y. Zhao, Integration of nanoassembly functions for an effective delivery cascade for cancer drugs, *Adv. Mater.*, 2014, **16**, 7615–7621.
3 S. Behera, P. Mohanty, P. Parimita, P. Mohapatra, L. Shubhadarshinee, R. Bechura, A. Kumar Barick, P. Mohapatra and B. R. Jali, Selective binding of bovine serum albumin (BSA): A comprehensive review, *Biointerface Res. Appl. Chem.*, 2023, **6**, 555.
4 W. Zhang, Q. Cheng, S. Guo, D. Liang, P. Huang, J. Liu, T. Wei, L. A. Deng, Z. Liang, X.-J. Liang and A. Dong, Gene transfection efficacy and biocompatibility of polycation/DNA complexes coated with enzyme degradable PEGylated hyaluronic acid, *Biomaterials*, 2013, **34**, 6495–6503.
5 X. Yao, C. Qi, C. Sun, F. Huo and X. Jiang, Poly(ethylene glycol) alternatives in biomedical applications, *Nano Today*, 2023, **48**, 101738.
6 A. Kolate, D. Baradia, S. Patil, I. Vhora, G. Kore and A. Misra, PEG - a versatile conjugating ligand for drugs and drug delivery systems, *J. Controlled Release*, 2014, **192**, 67–81.
7 E. Padín-González, P. Lancaster, M. Bottini, P. Gasco, L. Tran, B. Fadeel, T. Wilkins and M. P. Monopoli, Understanding the role and Impact of Poly(ethylene glycol) (PEG) on nanoparticle formulation: implications for COVID-19 vaccines, *Front. Bioeng. Biotechnol.*, 2022, **10**, 882363.
8 C. S. Fishburn, The Pharmacology of PEGylation: Balancing PD with PK to Generate Novel Therapeutics, *J. Pharm. Sci.*, 2008, **97**, 4167–4183.
9 J. C. Flores, G. F. Silbestri and E. de Jesús, Water-soluble transition-metal complexes with hydrophilic N-heterocyclic carbene ligands for aqueous-phase applications, in *Advances in Organometallic Chemistry*, Elsevier, 2022, ch. 4, vol. 77.
10 B. Lin, X. Zhang, C.-Y. Zhou and C.-M. Che, PEGylated N-heterocyclic carbene-gold(I) complex: an efficient catalyst for cyclization reaction in water, *Org. Chem. Front.*, 2021, **8**, 1216–1222.
11 M. J. MacLeod and J. A. Johnson, PEGylated N-heterocyclic carbene anchors designed to stabilize gold nanoparticles in biologically relevant media, *J. Am. Chem. Soc.*, 2015, **137**, 7974–7977.
12 J. P. Gallivan, J. P. Jordan and R. H. Grubbs, A neutral, water-soluble olefin metathesis catalyst based on an *N*-heterocyclic carbene ligand, *Tetrahedron Lett.*, 2005, **46**, 2577–2580.
13 C. Kim and H. Chung, Oligo(ethylene glycol) Length Effect of Water-Soluble Ru-Based Olefin Metathesis Catalysts on Reactivity and Removability, *J. Org. Chem.*, 2018, **83**, 9787–9794.
14 S. P. Y. Li, H. W. Liu, K. Y. Zhang and K. K. W. Lo, Modification of Luminescent Iridium(III) Polypyridine Complexes with Discrete Poly(ethylene glycol) (PEG) Pendants: Synthesis, Emissive Behavior, Intracellular Uptake, and PEGylation Properties, *Chem. – Eur. J.*, 2010, **16**, 8329–8339.
15 O. Barrios, C. Inclán, P. Herrera, A. Bort, A. Martín, J. Cano, I. Díaz-Laviada and R. Gómez, Ruthenium(II) complexes containing PEGylated N-heterocyclic carbene ligands for tunning biocompatibility in the fight against cancer, *J. Inorg. Biochem.*, 2025, **262**, 112765.

16 J. P. Gallivan, J. P. Jordan and R. H. Grubbs, A neutral, water-soluble olefin metathesis catalyst based on an *N*-heterocyclic carbene ligand, *Tetrahedron Lett.*, 2005, **46**, 2577–2580.
17 K. C. Ferreira Dantas, J. dos Santos Rosário and P. Pereira Silva-Caldeira, Polymeric Nanosystems applied for metal-based drugs and photosensitizers delivery: the state of the art and recent advancements, *Pharmaceutics*, 2022, **14**, 1596.
18 S. Swaminathan, R. Jayakumarti and R. Karvembu, Interweaving catalysis and cancer using Ru- and Os-arene complexes to alter cellular redox state: A structure-activity relationship (SAR) review, *Coord. Chem. Rev.*, 2023, **491**, 215230.
19 C. C. James, B. de Bruin and J. N. H. Reek, Transition metal catalysis in living cells: Progress, challenges and novel supramolecular solutions, *Angew. Chem., Int. Ed.*, 2023, **62**, 3202306645.
20 S. Banerjee and P. J. Sadler, Transfer hydrogenation catalysis in cells, *RSC Chem. Biol.*, 2021, **2**, 12–29.
21 M. Salmain, G. Gaschard, M. Baroud, E. Lepeltier, G. Jaouuuuen, C. Passirani and A. Vessieres, Thioredoxin Reductase and Organometallic Complexes: A Pivotal System to Tackle Multidrug Resistant Tumors?, *Cancer*, 2023, **18**, 4448.
22 D. Wang and D. Astruc, The Golden Age of Transfer Hydrogenation, *Chem. Rev.*, 2015, **115**, 6621–6686.
23 B. Taleb, R. Jahjah, D. Cornu, M. Bechelany, M. Al Ajami, G. Kataya, A. Hijazi and M. H. El-Dakdouki, Exploring Hydrogen Sources in Catalytic Transfer Hydrogenation: A Review of Unsaturated Compound Reduction, *Molecules*, 2023, **29**, 7541–7575.
24 D. A. Hey, R. B. Reich, W. Baratta and F. E. Kün, Current advances on ruthenium(II) N-heterocyclic carbenes in hydrogenation reactions, *Coord. Chem. Rev.*, 2018, **374**, 114–132.
25 M. Kaloğlu, N. Gurbuz, D. Semeril and İ. Ozdemir, Ruthenium(II)-(*p*-cymene)-N-Heterocyclic Carbene Complexes for the *N*-Alkylation of Amine Using the Green Hydrogen Borrowing Methodology, *Eur. J. Inorg. Chem.*, 2018, 1236–1243.
26 W. Streciwilk, A. Terenzi, X. Cheng, L. Hager, Y. Dabiri, P. Prochnow, J. E. Bandow, S. Wolfl, B. K. Keppler and I. Ott, Fluorescent organometallic rhodium(I) and ruthenium(II) metallodrugs with 4-ethylthio-1,8-naphthalimide ligands: Antiproliferative effects, cellular uptake and DNA-interaction, *Eur. J. Med. Chem.*, 2018, **156**, 148–161.
27 K. M. Waldie, A. L. Osterichter, M. H. Teineke, A. F. Sasayama and C. P. Kubiak, Hydricity of transition-metal hydrides: thermodynamic considerations for CO_2 reduction, *ACS Catal.*, 2018, **8**, 1313–1324.
28 C. Li and T. Arakawa, Application of native polyacrylamide gel electrophoresis for protein analysis: Bovine serum albumin as a model protein, *Int. J. Biol. Macromol.*, 2019, **125**, 566–571.
29 J. Liu, Y. He, D. Liu, Y. He, Z. Tang, H. Lou, Y. Huo and X. Cao, Characterizing the binding interaction of astilbin with bovine serum albumin: a spectroscopic study in combination with molecular docking technology, *RSC Adv.*, 2018, **8**(13), 7280–7286.
30 J. Ashley and P. Manikova, Fluorescent sensors, in *Fundamentals of Sensor Technology: Principles and Novel Designs*, 2023, pp. 147–161.
31 M. Grodzicka, S. Michlewska, A. Buczkowski, S. Sekowski, C. E. Pena-Gonzalez, P. Ortega, F. J. De la Mata, J. Blasiak, M. Bryszewska and M. Ionov, A new class of polyphenolic carbosilane dendrimers binds human serum albumin in a structure-dependent fashion, *Sci. Rep.*, 2024, **14**(1), 1–9.
32 Z. Guo, Z. Kong, Y. Wei, H. Li, Y. Wang, A. Huang and L. Ma, Effects of gene carrier polyethyleneimines on the structure and binding capability of bovine serum albumin, *Spectrochim. Acta, Part A*, 2017, **173**, 783–791.
33 A. Vinothini, C. Vedhi, A. Mathavan, E. Arulkumar and S. Thanikaikarasan, Biosynthesis of Cd and Ru doped CeO_2 nanoparticles with enhanced biomedical applications, *Results Chem.*, 2024, **7**, 101243.
34 Y. Liu, Q. Yu, C. Wang, D. Sun, Y. Huang, Y. Zhou and J. Liu, Ruthenium(II) complexes binding to human serum albumin and inducing apoptosis of tumor cells, *Inorg. Chem. Commun.*, 2012, **24**, 104–109.
35 A. T. Buddanavar and S. T. Nandibewoor, Multi-spectroscopic characterization of bovine serum albumin upon interaction with atomoxetine, *J. Pharm. Anal.*, 2017, **7**(3), 148–155.
36 K. P. Fears, C. T. Love and D. E. Day, Albumin conformational change and aggregation induced by nanostructured apatites, *Biointerphases*, 2017, **12**(2), 02D403.
37 M. Hołota, J. Magiera, S. Michlewska, M. Kubczak, N. S. del Olmo, S. García-Gallego, P. Ortega, F. J. de la Mata, M. Ionov and M. Bryszewska, In vitro anticancer properties of copper metallodendrimers, *Biomolecules*, 2019, **9**(4), 1–15.
38 B. Jachimska and A. Pajor, Physico-chemical characterization of bovine serum albumin in solution and as deposited on surfaces, *Bioelectrochemistry*, 2012, **87**, 138–146.
39 Y. J. P. Carreón, A. M. Jaramillo-Granada, D. Fuentes-López, A. D. Reyes-Figueroa, J. González-Gutiérrez and H. Mercado-Uribe, Bovine serum albumin under the influence of alkali metal halides, *RSC Adv.*, 2025, **15**(1), 244–251.
40 H. A. Alhazmi, W. Ahsan, A. M. M. Ibrahim, R. A. Y. Khubrani, Z. A. A. Haddadi, A. Y. F. Safhi, N. Shubayr, M. Al Bratty and A. Najmi, Investigation of bovine serum albumin aggregation upon exposure to silver (I) and copper(II) metal ions using Zetasizer, *Open Chem.*, 2021, **19**(1), 987–997.
41 S. Sengottiyan, A. Mikolajczyk, K. Jagiełło, M. Swirog and T. Puzyn, Core, Coating, or Corona? The Importance of Considering Protein Coronas in nano-QSPR Modeling of Zeta Potential, *ACS Nano*, 2023, **17**, 1989–1997.
42 D. A. Herold, K. Keil and D. E. Bruns, Oxidation of polyethylene glycols by alcohol dehydrogenase, *Biochem. Pharmacol.*, 1989, **38**, 73–76.

43 R. Webster, V. Elliott, B. K. Park, D. Walker, M. Hankin and P. Taupin, *PEGylated protein drugs: Basic science and clinical applications*, Springer Science & Business Media, 2009, pp. 127–146.

44 J. DePasquale, M. Kumar, M. Zeller and E. T. Papish, Variations on an NHC Theme: Which Features Enhance Catalytic Transfer Hydrogenation with Ruthenium Complexes?, *Organometallics*, 2013, **32**, 966–979.

45 S. Betanzos-Lara, Z. Liu, A. Habtemariam, A. M. Pizarro, B. Qamar and P. J. Sadler, Organometallic ruthenium and iridium transfer-hydrogenation catalysts using coenzyme NADH as a cofactor, *Angew. Chem., Int. Ed.*, 2012, **51**, 3897–3900.

46 J. J. Soldevila-Barreda, P. C. A. Bruijnincx, A. Habtemariam, G. J. Clarkson, R. J. Deeth and P. J. Sadler, Improved catalytic activity of ruthenium–arene complexes in the reduction of NAD+, *Organometallics*, 2012, **31**, 5958–5967.

47 G. Mencia, S. Algar, T. Lozano-Cruz, M.ª. A. Muñoz-Fernández, E. R. Gillies, J. Cano, M. Valiente and R. Gómez, Carbosilane Dendritic Amphiphiles from Cholesterol or Vitamin E for Micelle Formation, *Pharmaceutics*, 2024, **16**, 451.

48 M. Viciano-Chumillas, M. Mon, J. Ferrando-Soria, A. Corma, A. Leyva-Pérez, D. Armentano and E. Pardo, Metal-organic frameworks as chemical nanoreactors: synthesis and stabilization of catalytically active metal species in confined spaces, *Acc. Chem. Res.*, 2020, **53**, 520–531.

49 P. Ferri, C. Li, C. Paris, A. Vidal-Moya, M. Moliner, M. Boronat and A. Corma, Chemical and structural parameter connecting cavity architecture, confined hydrocarbon pool species, and MTO product selectivity in small-pore cage-based zeolites, *ACS Catal.*, 2019, **9**, 11542–11551.

50 A. K. Rappé, C. J. Casewit, K. S. Colwell, W. A. Goddard and W. M. Skiff, UFF, a full periodic table force field for molecular mechanics and molecular dynamics simulations, *J. Am. Chem. Soc.*, 1992, **114**, 10024–10035.

51 A. K. Rappé and W. A. Goddard, Charge equilibration for molecular dynamics simulations, *J. Phys. Chem.*, 1991, **95**, 3358–3363.

52 J. C. Berendsen, J. R. Grigera and T. P. Straatsma, The missing term in effective pair potentials, *J. Phys. Chem.*, 1987, **91**(24), 6269–6271.

53 S. Nosé, A molecular dynamics method for simulations in the canonical ensemble, *Mol. Phys.*, 1984, **52**, 255–268.

54 H. C. Andersen, Molecular dynamics simulations at constant pressure and/or temperature, *J. Chem. Phys.*, 1980, **72**, 2384–2393.

55 E. F. Pettersen, T. D. Goddard, C. C. Huang, G. S. Couch, D. M. Greenblatt, E. C. Meng and T. E. Ferrin, UCSF Chimera - A Visualization System for Exploratory Research and Analysis, *J. Comput. Chem.*, 2004, **13**, 1605–1612.